

# VPOcc: Exploiting Vanishing Point for Monocular 3D Semantic Occupancy Prediction

Junsu Kim<sup>1</sup>, Junhee Lee<sup>1</sup>, Ukcheol Shin<sup>2</sup>, Jean Oh<sup>2</sup> and Kyungdon Joo<sup>1,†</sup>

**Abstract**—Monocular 3D semantic occupancy prediction is becoming important in robot vision due to the compactness of using a single RGB camera. However, existing methods often do not adequately account for camera perspective geometry, resulting in information imbalance along the depth range of the image. To address this issue, we propose a vanishing point (VP) guided monocular 3D semantic occupancy prediction framework named **VPOcc**. Our framework consists of three novel modules utilizing VP. First, in the VPZoomer module, we initially utilize VP in feature extraction to achieve information balanced feature extraction across the scene by generating a zoom-in image based on VP. Second, we perform perspective geometry-aware feature aggregation by sampling points towards VP using a VP-guided cross-attention (VPCA) module. Finally, we create an information-balanced feature volume by effectively fusing original and zoom-in voxel feature volumes with a balanced feature volume fusion (BFVF) module. Experiments demonstrate that our method achieves state-of-the-art performance for both IoU and mIoU on SemanticKITTI and SSCBench-KITTI360. These results are obtained by effectively addressing the information imbalance in images through the utilization of VP. Our code will be available at [www.github.com/anonymous](https://www.github.com/anonymous).

## I. INTRODUCTION

Comprehensive 3D scene understanding is a crucial challenge within robot systems or intelligent agents for making accurate and efficient decisions in tasks, such as path planning and navigation [1], [2]. 3D semantic occupancy prediction, which recognizes what an object is (*i.e.*, classification) and what area is occupied (*i.e.*, occupancy), is one research branch to achieve 3D semantic and spatial understanding simultaneously [3], [4]. This literature initially relies on explicit distance measuring sensors, such as LiDAR and RGB-D sensors [3], [5], [6]. However, research has expanded to perform 3D semantic occupancy prediction only utilizing a single RGB camera [7], [8], [9], thanks to its affordability and compactness.

Camera-based 3D semantic occupancy prediction is considered a challenging task because it relies entirely on 2D images. Concretely, several ambiguities can occur since this task needs to reconstruct or understand 3D space only from single or multi-view 2D images, such as missing metric-scale depth [7], feature dimension mismatch [8], [10], [9] and occlusion [11], [12]. Basically, these issues are closely related to the perspective geometry of the camera.

<sup>1</sup>Junsu Kim, Junhee Lee and Kyungdon Joo are with the Artificial Intelligence Graduate School, UNIST, Ulsan, South Korea. [{joonsu0109, junhee98, kyungdon}@unist.ac.kr](mailto:{joonsu0109, junhee98, kyungdon}@unist.ac.kr)

<sup>2</sup>Ukcheol Shin and Jean Oh are with Robotics Institute, Carnegie Mellon University, Pittsburgh, Pennsylvania, 15217, United States. [{ushin, hyaejino}@andrew.cmu.edu](mailto:{ushin, hyaejino}@andrew.cmu.edu)

<sup>†</sup>Corresponding author

The process of generating an image (*i.e.*, perspective geometry) involves projecting 3D scenes onto an image plane, resulting in distant objects in 3D space appearing smaller than nearby objects in 2D image space [13]. As a result, the image usually contains dense information at close distance objects, but it provides insufficient density for the far objects, which is an imbalance in information density. The difference is more apparent in outdoor than indoor environments. For example, as shown in Fig. 1, the nearby object (green) and the distant object (red) have a similar size in 3D space. However, in 2D space, the nearby object has a ten times greater resolution than the distant object due to the camera perspective projection. In particular, this imbalanced information density leads to imbalanced feature extraction and poor performance. To resolve this issue, there are several attempts using deformable operations, such as deformable convolution [14], which introduces learnable offsets to address the limitation of the fixed receptive field in convolution and extends to attention mechanisms [15]. However, the implicit strategy may be insufficient to account for information imbalance caused by the perspective geometry.

In this work, we exploit a vanishing point (VP), a 2D point on the horizon line where parallel lines in 3D space appear to converge, as shown in Fig. 1. Specifically, VP is a 2D geometric cue that reflects perspective geometry and usually indicates distant areas in a given image, especially in road environments. Thus, by utilizing VP in a given image, we can explicitly distinguish whether a specific region in an image corresponds to near and far areas. Based on the fact that VP explicitly encodes the perspective geometry, we propose a VP-guided 3D semantic occupancy prediction framework named **VPOcc**. The proposed framework contains three novel modules utilizing VP: VPZoomer, VP-guided cross-attention (VPCA) module, and balanced feature volume fusion (BFVF) module. Our contributions are summarized as follows:

- We propose a novel VPZoomer to synthesize a zoom-in image toward VP, enabling us to obtain distance-balanced information about near and far areas.
- We present a new VPCA module that extracts sampling points toward VP while considering the camera perspective geometry. It enables the aggregating of 2D features suitable for 3D voxel queries.
- Using a BFVF module, we effectively fuse and refine voxel feature volumes from the original and zoom-in images.

### Problem: Imbalanced information



### Solution: Exploiting Vanishing Point for Monocular 3D Semantic Occupancy Prediction

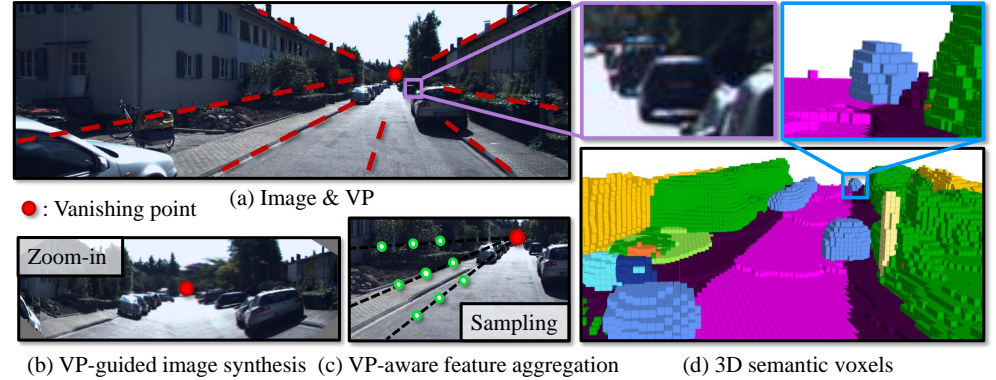


Fig. 1: **Overview of the proposed VPOCC.** To address the information imbalance in 2D images caused by camera perspective projection (e.g., vehicles of similar sizes in 3D appearing with different scales in 2D), we explicitly utilize vanishing point (VP) for 3D semantic occupancy prediction. (a) Given an input image and VP, we perform (b) VP-guided image synthesis with zoom-in and (c) VP-guided point sampling for feature aggregation. These strategies enable us to compose a balanced voxel feature volume, resulting in an accurate estimation of 3D semantic voxels for the scene across the depth range, including distant objects.

- We demonstrate that our proposed framework, VPOCC, outperforms previous methods on the SemanticKITTI [16] and SSCBench-KITTI360 [17] datasets, with extensive ablation studies proving its effectiveness.

## II. RELATED WORK

### A. Camera-based 3D semantic occupancy prediction

3D semantic occupancy prediction, also known as 3D semantic scene completion (SSC), aims to predict complete occupancy and semantics simultaneously based on incomplete scene data. SSCNet [3] is the first work to define the SSC task from a single RGB-D frame. Based on SSCNet, several studies utilize the 3D sensor data to improve 3D SSC tasks [6], [5].

Recently, camera-based 3D occupancy prediction has attracted significant attention in robot vision. MonoScene [7] is the first attempt to use only a monocular image. By projecting 3D voxels onto a 2D feature map and aggregating features, MonoScene completes the 3D scene based on 2D images. Following MonoScene, several studies have been developed to predict 3D semantic occupancy from a monocular image, focusing on effectively composing 3D voxel feature volume. VoxFormer [8] involves constructing a voxel query based on estimated depth from an image and then lifting a 2D feature map into a 3D voxel feature using cross-attention to place image features more accurately. OccFormer [11] estimates a 3D voxel grid using the depth distribution of an image feature map and then employs a transformer-based decoder for completion.

### B. Geometry as priors

Unlike previous works focusing on constructing the 3D feature volume and the decoder itself, the proposed VPOCC explicitly utilizes a VP to consider perspective geometry within the 3D semantic occupancy prediction. For a long time, many fields have persistent efforts to use

geometry as prior information [18], [19], [20]. In object detection, incorporating prior maps for image height [21] or converting image depth to point clouds using camera parameters [18] has been used to overcome the limitations of 2D images. In the domain of semantic segmentation, there have been attempts to identify distant areas that are difficult to segment with perspective-aware techniques [20] and distilling information from depth into the segmentation network to inject a 3D geometry prior [19]. In the field of depth estimation, there have been approaches utilizing the camera motion between a stereo pair for unsupervised learning or considering the slanted angle of a fisheye camera to construct a feature space that is orthogonal to the ground [22].

In monocular 3D semantic occupancy prediction, careful consideration of geometry is crucial for constructing a 3D scene from a 2D image. To address this, we use VP as geometric prior information to handle the scale variance resulting from the camera perspective projection from 3D to 2D.

### C. Image processing via zoom-in

The lack of features in small regions of an image is a challenging issue [23], [24]. One of the most intuitive methods is to zoom-in on the image, thereby enlarging small objects [25]. One approach is resampling the image to enlarge the desired areas [26], [27]. Another approach utilizes saliency maps to zoom-in on the image [26]. Additionally, leveraging both the upper and lower image planes in road environments to enhance the detection of small objects [27].

Existing methods usually focus on 2D tasks. In contrast, monocular 3D semantic occupancy prediction requires a geometrically structured approach to accurately estimate 3D scenes from a 2D image. Our VPZoomer uses homography warping to create zoomed-in images while preserving the geometric structure as much as possible.

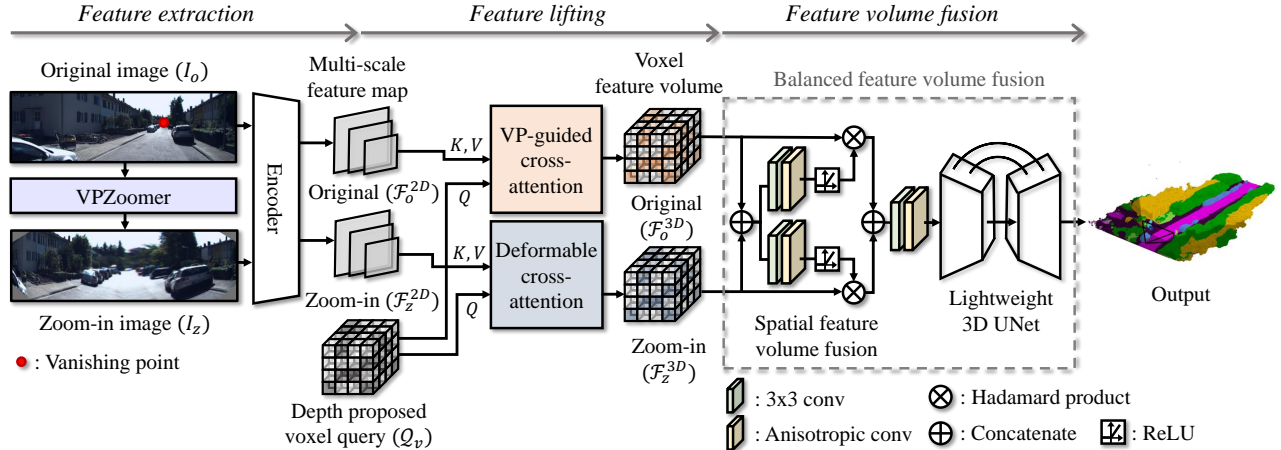


Fig. 2: **Overall architecture.** VPOCC consists of three sequential parts. In the feature extraction step, using VPZoomer, we extract the multi-scale feature maps  $\mathcal{F}_o^{2D}$  and  $\mathcal{F}_z^{2D}$  from  $I_o$  and  $I_z$ . In the feature lifting step, we use the depth-proposed voxel query  $\mathcal{Q}_v$  with VP-guided cross-attention and deformable cross-attention to construct voxel feature volumes  $\mathcal{F}_o^{3D}$  and  $\mathcal{F}_z^{3D}$ . In the feature volume fusion step, we combine both  $\mathcal{F}_o^{3D}$  and  $\mathcal{F}_z^{3D}$  using a spatial feature volume fusion network and refine them using the lightweight 3D UNet decoder on the balanced feature volume fusion.

### III. METHOD

We propose a VP-guided 3D semantic occupancy prediction framework, VPOCC. Our method takes a monocular image, the corresponding VP, and depth<sup>1</sup> to estimate accurate 3D semantic occupancy. In particular, we focus on explicitly exploiting VP in the framework. In the following, we present the overall pipeline and the details of key modules in VPOCC.

#### A. Overview

The proposed method addresses the problem of monocular 3D semantic occupancy prediction based on VP (see Fig. 2). Our framework mainly consists of three parts: feature extraction, feature lifting, and feature volume fusion, where VP is seamlessly integrated into this framework.

**Feature extraction.** For a given input image  $I_o \in \mathbb{R}^{H \times W \times 3}$ , we propose a VP-based image zoom-in module, VPZoomer, that generates a zoom-in image  $I_z \in \mathbb{R}^{H \times W \times 3}$  based on a given VP. We then use a panoptic segmentation pre-trained encoder [29] to create multi-scale feature maps  $\mathcal{F}_o^{2D}$  and  $\mathcal{F}_z^{2D}$  for each of  $I_o$  and  $I_z$ . By using both the original and zoomed-in images, we extract balanced features across the scene, handling the information imbalance caused by the perspective projection at the input level.

**Feature lifting.** We construct a depth proposed voxel query  $\mathcal{Q}_v$ , following Symphonies [12]. To compose  $\mathcal{Q}_v$ , we first initialize the weights of the voxel grid, shaped as  $\mathcal{F}^{3D} \in \mathbb{R}^{X \times Y \times Z \times C}$ . Then, back-projects the estimated depth map to a 3D point cloud using camera parameters. After that, we fill the voxel query  $\mathcal{Q}_v$  with the overlapped point cloud. With  $\mathcal{Q}_v$ , we aggregate the multi-scale image features via cross-attention. In this process, our VP-guided cross-attention (VPCA) module that samples points towards VP is employed for  $\mathcal{F}_o^{2D}$ , as explained in Sec. III-C.

<sup>1</sup>Following VoxFormer [8] and Symphonize [12], we use the pre-trained depth estimation network [28] to construct depth-proposed voxel queries.

Meanwhile, we utilize the general deformable cross-attention (DCA) [15] for  $\mathcal{F}_z^{2D}$  to complement the output of VPCA. To compute the attention results,  $N$  sampling points  $\mathbf{p}$  are selected around the reference point  $\mathbf{r}$ . Subsequently, the proposed depth voxel query  $\mathbf{q}_v$  will be refined with the following mathematical equation:

$$\text{DCA}(\mathbf{q}_v, \mathbf{r}, \mathcal{F}_z^{2D}) = \sum_{i=1}^N \mathbf{A}_{\mathbf{q}_v} \mathbf{W}_i \mathcal{F}_z^{2D}(\mathbf{p}_i + \delta\mathbf{p}_i). \quad (1)$$

As a result, we obtain the voxel feature volumes  $\mathcal{F}_o^{3D}$  and  $\mathcal{F}_z^{3D}$  for the original and zoom-in.

**Feature volume fusion.**  $\mathcal{F}_o^{3D}$  and  $\mathcal{F}_z^{3D}$  are fused through a balanced feature volume fusion (BFVF) module, including a spatial feature volume fusion module and a lightweight 3D UNet based decoder. The fusion of  $\mathcal{F}_o^{3D}$  and  $\mathcal{F}_z^{3D}$  creates a balanced feature volume that encompasses both near and far areas. Then, the composed feature volume is upsampled with 3D deconvolution to match the resolution of the label and processed through a segmentation head with  $1 \times 1$  3D convolution to predict the final output.

**Training objective.** We use depth [28] and VP [30] inferred from images, and the pre-trained panoptic segmentation encoder [29]. Following MonoScene [7], we use scene-class affinity loss  $\mathcal{L}_{\text{scal}}$  for class-wise metrics, with  $\mathcal{L}_{\text{scal}}^{\text{sem}}$  and  $\mathcal{L}_{\text{scal}}^{\text{geo}}$  for geometry and semantics. We also used cross-entropy loss  $\mathcal{L}_{\text{ce}}$ , weighted by class frequencies, for occupancy prediction. The total loss is formulated as:

$$\mathcal{L} = \mathcal{L}_{\text{scal}}^{\text{geo}} + \mathcal{L}_{\text{scal}}^{\text{sem}} + \mathcal{L}_{\text{ce}}. \quad (2)$$

#### B. VPZoomer: Vanishing point-based image zoom-in

Camera perspective projection causes near areas to appear larger and far areas to appear smaller in the image, leading to an information imbalance along the depth. To resolve this issue at the input level, our VPZoomer generates the zoom-in image  $I_z$  toward VP, as shown in Fig. 3.

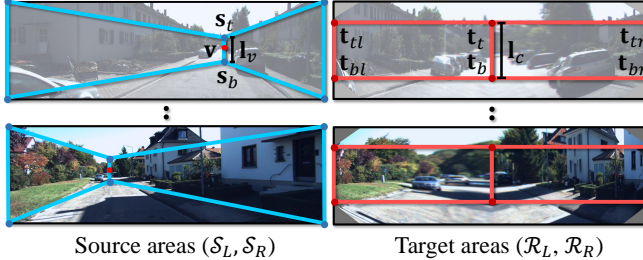


Fig. 3: **Illustration of VPZoomer.** Given VP  $\mathbf{v}$  and the input image  $I_o$ , VPZoomer calculates VP-centric source areas and image-centric target areas, estimates each homography matrix, and warps the source areas to the target areas.

Given the original image  $I_o$  and VP  $\mathbf{v} = [v_x, v_y]^\top$ , VPZoomer warps two source areas with trapezoidal shapes (blue) to target areas of rectangular shapes (red) by 2D transformation. It should be noted that we use trapezoids as the shape of the source areas, not triangles stemming from VP, because trapezoids produce less distortion than triangles, and their four vertices allow us to compute homography between source and target regions directly. Specifically, we first need to define a shared vertical line to construct two trapezoids with a ribbon shape based on VP.

Thus, we define this shared vertical line  $\mathbf{l}_v$  as a vertical line segment centered at VP  $\mathbf{v}$  and with a length of  $\alpha \cdot H$ , where  $\alpha$  is the scaling factor. Here, we describe this line segment by two endpoints, top  $\mathbf{s}_t$  and bottom  $\mathbf{s}_b$ :

$$\mathbf{s}_t = [v_x, v_y - \frac{\alpha \cdot H}{2}]^\top, \quad \mathbf{s}_b = [v_x, v_y + \frac{\alpha \cdot H}{2}]^\top. \quad (3)$$

Based on top  $\mathbf{s}_t$  and bottom  $\mathbf{s}_b$  constructing  $\mathbf{l}_v$ , we can now represent two trapezoids, left  $\mathcal{S}_L$  and right trapezoid  $\mathcal{S}_R$  of source areas, as a set of four vertices. Let  $\mathbf{x}_{tl}$ ,  $\mathbf{x}_{tr}$ ,  $\mathbf{x}_{bl}$ , and  $\mathbf{x}_{br}$ <sup>2</sup> be a set of corner vertices of the image. We can define two trapezoids as:

$$\mathcal{S}_L = \{\mathbf{x}_{tl}, \mathbf{s}_t, \mathbf{s}_b, \mathbf{x}_{bl}\}, \quad \mathcal{S}_R = \{\mathbf{s}_t, \mathbf{x}_{tr}, \mathbf{x}_{br}, \mathbf{s}_b\}. \quad (4)$$

In the case of target areas, it should have balanced information density regardless of distance and left-and-right asymmetry. Thus, we define the target areas as two rectangles, left  $\mathcal{R}_L$  and right  $\mathcal{R}_R$ , with a width of  $W/2$ . In other words, two rectangles share a vertical line  $\mathbf{l}_c$  at the image center to have the balanced information density regardless of the two trapezoids of source areas. Here, we also describe this line segments  $\mathbf{l}_c$  by two endpoints, top  $\mathbf{t}_t$  and bottom  $\mathbf{t}_b$ , and we stretch its length along the y-axis to have more pixel density at distant regions:

$$\mathbf{t}_t = [\frac{W}{2}, \frac{s_{ty}}{2}]^\top, \quad \mathbf{t}_b = [\frac{W}{2}, \frac{H + s_{by}}{2}]^\top. \quad (5)$$

By using two points  $\mathbf{t}_t$  and  $\mathbf{t}_b$ , we can define two rectangles similarly to Eq. (4):

$$\mathcal{R}_L = \{\mathbf{t}_{tl}, \mathbf{t}_t, \mathbf{t}_b, \mathbf{t}_{bl}\}, \quad \mathcal{R}_R = \{\mathbf{t}_t, \mathbf{t}_{tr}, \mathbf{t}_{br}, \mathbf{t}_b\}, \quad (6)$$

where  $\mathbf{t}_{tl} = [0, t_{ty}]^\top$ ,  $\mathbf{t}_{tr} = [W, t_{ty}]^\top$ ,  $\mathbf{t}_{bl} = [0, t_{by}]^\top$ , and  $\mathbf{t}_{br} = [W, t_{by}]^\top$ . Note that  $t_{ty}$  and  $t_{by}$  represent the y values of  $\mathbf{t}_t$  and  $\mathbf{t}_b$  in Eq. (5), respectively.

<sup>2</sup>Subscript  $l$ ,  $r$ ,  $t$  and  $b$  indicate left, right, top and bottom, respectively.

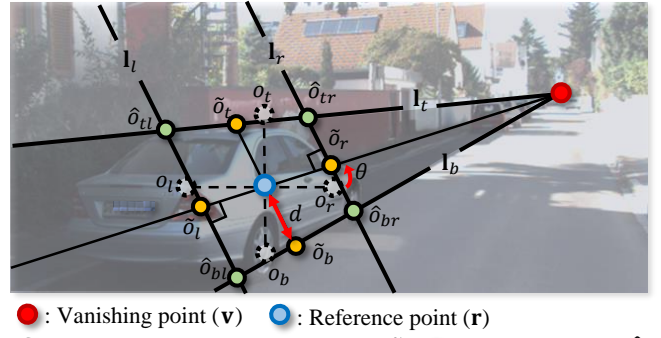


Fig. 4: **VP-guided point sampling.** Centered on reference point  $\mathbf{r}$ , we generate the initial grid  $\mathcal{O}$  and rotate it by angle  $\theta$  to obtain  $\tilde{\mathcal{O}}$ . We then identify the intersection grid  $\hat{\mathcal{O}}$  at the cross-point of lines from  $\tilde{\mathcal{O}}$  and VP  $\mathbf{v}$ . Additionally, we scale the offset  $d$  according to the feature map resolution.

After constructing correspondences between source and target (*i.e.*,  $[\mathcal{S}_L, \mathcal{R}_R]$  and  $[\mathcal{S}_R, \mathcal{R}_L]$ ), we then compute each homography transformation  $\mathbf{H}_L$  and  $\mathbf{H}_R$  by solving singular value decomposition (SVD) [13]. Lastly, the VP-guided zoom-in image  $I_z$  is composited by the following process:

$$I_z = \mathbf{M} \odot I_l + (1 - \mathbf{M}) \odot I_r, \quad (7)$$

where  $I_r = \mathbf{H}_R(I_o)$ ,  $I_l = \mathbf{H}_L(I_o)$ ,

where  $\mathbf{M}$  is a binary mask that activates the left-half area ( $H \times W/2$ ),  $1 - \mathbf{M}$  activates the remaining half area,  $\odot$  indicates element-wise multiplication, and  $\mathbf{H}_L(\cdot)$  and  $\mathbf{H}_R(\cdot)$  represent warping functions.

Through the process described, VPZoomer creates an image zoom-in towards VP, which is  $I_z$ , providing a richer detail of distant areas than what is available in the original image  $I_o$ .

### C. VP-guided cross-attention

When constructing a 3D feature volume by aggregating 2D image features implicitly with deformable cross-attention, the camera perspective geometry is not adequately considered [8], [12]. To address this, we propose the VP-guided cross-attention (VPCA) module that samples grid points with a trapezoidal shape towards VP. This approach ensures that points are sampled appropriately for the reference point, considering camera perspective projection.

**VP-guided point sampling.** Given a reference point  $\mathbf{r} = [r_x, r_y]^\top$  and VP  $\mathbf{v}$ , VP-guided sampling aims to extract sample grid points  $\mathcal{P}$  by considering the distance and radial form from  $\mathbf{v}$  to  $\mathbf{r}$ . Specifically, we first extract cross-shaped initial grid points  $\mathcal{O}$  (see Fig. 4), where we set the offset as the distance  $d$  between  $\mathbf{v}$  and  $\mathbf{r}$ :

$$d = c \|\mathbf{v} - \mathbf{r}\|_2^2, \quad (8)$$

where  $c$  indicates scale parameter according to the resolution of feature  $\mathcal{F}_o^{2D}$ . Afterward, the offset is bounded in the range of  $[0, \beta]$  to prevent an abnormal increase.

Based on  $d$ , we define  $\mathcal{O} = \{\mathbf{o}_l, \mathbf{o}_r, \mathbf{o}_t, \mathbf{o}_b\}$  with the offset along each axis. For example,  $\mathbf{o}_l = [r_x - d, r_y]^\top$  and

$\mathbf{o}_t = [r_x, r_y - d]^\top$  represent left grid and top grid points, respectively. Then, using the angle formed by  $\mathbf{v} - \mathbf{r}$  and the x-axis, we rotate  $\mathcal{O}$  so that it is aligned with  $\mathbf{v}$ .

We denote these rotated initial grid points as  $\tilde{\mathcal{O}}$ . Specifically, we compute the angle  $\theta$  by  $\text{atan2}(v_y - r_y, v_x - r_x)$  and then rotate each point  $\mathbf{o} \in \mathcal{O}$ :

$$\tilde{\mathbf{o}} = \mathbf{R}\mathbf{o}, \text{ where } \mathbf{R}_\theta = \begin{bmatrix} \cos \theta & -\sin \theta \\ \sin \theta & \cos \theta \end{bmatrix}. \quad (9)$$

These rotated grid points  $\tilde{\mathcal{O}} = \{\tilde{\mathbf{o}}_l, \tilde{\mathbf{o}}_r, \tilde{\mathbf{o}}_t, \tilde{\mathbf{o}}_b\}$  correspond to cross-shaped sample points that reflect a given  $\mathbf{v}$  (see yellow points in Fig. 4). Afterwards, we compute a line  $\mathbf{l}_t$  that passes through  $\mathbf{v}$  and  $\tilde{\mathbf{o}}_t$  by  $\mathbf{v} \times \tilde{\mathbf{o}}_t$  and the same goes for a line  $\mathbf{l}_b$  by  $\mathbf{v} \times \tilde{\mathbf{o}}_b$ . From the direction vector  $\mathbf{d}$ , defined by subtracting  $\tilde{\mathbf{o}}_t$  and  $\tilde{\mathbf{o}}_b$ , we can generate another line  $\mathbf{l}_l$  that passes through  $\tilde{\mathbf{o}}_l$ , and the same goes a line  $\mathbf{l}_r$  for  $\tilde{\mathbf{o}}_r$ . Then, by computing the intersection points between lines (e.g.,  $\hat{\mathbf{o}}_{tl} = \mathbf{l}_l \times \mathbf{l}_t$ ), we can estimate intersection grid points  $\hat{\mathcal{O}} = \{\hat{\mathbf{o}}_{tl}, \hat{\mathbf{o}}_{tr}, \hat{\mathbf{o}}_{bl}, \hat{\mathbf{o}}_{br}\}$  that construct a trapezoid toward VP. As a result, we can sample a set of nine points  $\mathcal{P} = \{\hat{\mathcal{O}}, \hat{\mathcal{O}}, \mathbf{r}\}$  for each reference point  $\mathbf{r}$ . We use  $\mathcal{P}$  for the following VP-guided cross-attention.

**Feature aggregation by cross-attention.** VPCA aggregates image features at sampled point  $\mathcal{F}_o^{2D}(\mathbf{p})$ , where  $\mathbf{p} \in \mathcal{P}$ , with the depth proposed voxel query  $\mathbf{q}_v$ , where  $\mathbf{q}_v \in \mathcal{Q}_v$ , via cross-attention mechanism and produces voxel feature volume  $\mathcal{F}_o^{3D}$ :

$$\text{VPCA}(\mathbf{q}_v, \mathbf{r}, \mathcal{F}_o^{2D}) = \sum_{i=1}^N \mathbf{A}_{\mathbf{q}_v} \mathbf{W}_i \mathcal{F}_o^{2D}(\mathbf{p}_i), \quad (10)$$

where  $N$  is the numbers of sampling points ( $N = 9 \times 3$  due to multi-resolution of features) and  $\mathbf{A}_{\mathbf{q}_v}$  represents the attention matrix based on  $\mathbf{q}_v$ , and  $\mathbf{W}$  is weight matrix. Please kindly refer to the operation details here [15]. Note that we use default deformable cross-attention block for zoom-in feature  $\mathcal{F}_z^{2D}$  because the input image has balanced information density already, thanks to the VPZoomer. On the other hand, the original image feature  $\mathcal{F}_o^{2D}$  still has a perspective geometry effect, so we apply the VPCA module only to the original image feature map  $\mathcal{F}_o^{2D}$ . When constructing a 3D feature volume by aggregating 2D image features implicitly with deformable cross-attention, the camera perspective geometry may not be adequately considered [8], [12].

#### D. Balanced feature volume fusion

After the feature lifting process, we have two voxel feature volumes,  $\mathcal{F}_z^{3D}$  and  $\mathcal{F}_o^{3D}$ , which handle the perspective geometry effect in input and aggregation level, respectively. To aggregate these two feature volumes, we construct a balanced volume fusion (BFVF) module that produces voxel feature volumes with balanced features over near and far areas.

**Spatial feature volume fusion.** As shown in Fig. 2, it begins by generating two attention masks from the voxel feature volumes  $\mathcal{F}_o^{3D}$  and  $\mathcal{F}_z^{3D}$ . The concatenated feature volume feeds forward through a  $3 \times 3$  convolution layer

and an anisotropic convolution layer [31] to aggregate local and non-local representation. After that, each attention mask is generated via the ReLU activation layer and is multiplied with each feature volume  $\mathcal{F}_o^{3D}$  and  $\mathcal{F}_z^{3D}$  to highlight important voxel feature regions. Two attention-weighted volumes are concatenated and then fused by non-local aggregation. Lastly, the final result is estimated by passing through the lightweight 3D UNet inspired from [7].

## IV. EXPERIMENTS

In this section, we evaluate our VPOcc and conduct ablation studies to validate the effectiveness of our framework. In Sec. IV-A, we describe the experimental settings of our method. Sec. IV-B shows the superiority of our method through performance comparisons, and Sec. IV-C validates the effectiveness of our modules via ablation studies. We provide further experiments and visual examples of VPZoomer and VPCA modules, along with additional qualitative results in the supplementary video.

### A. Implementation details

**Datasets and metrics.** Our experiments are conducted on SemanticKITTI [16] and SSCBench-KITTI360 [17] datasets, which consist of 22 and 9 sequences, and 20 and 19 classes including the empty class. These datasets are composed of voxel grids with semantic labels over an area of  $51.2m \times 51.2m \times 6.4m$  using a  $0.2m$  voxel size, resulting in  $256 \times 256 \times 32$  voxel grids. Following the standard train/val/test splits [7], [12] with the hidden test set of SemanticKITTI, we use Intersection over Union (IoU) to assess class-agnostic completion quality and mean IoU (mIoU) to evaluate voxel semantic segmentation performance.

**Training setup.** Experiments are conducted using NVIDIA 3090 GPUs. Training with 4 GPUs, one batch per GPU, over 30 epochs takes approximately 16 hours to complete. We adopt the AdamW [34] optimizer, configured with a starting learning rate of  $2e-4$  and a weight decay parameter of  $1e-4$ . After reaching the 25th epoch, we adjust the learning rate by reducing it to 0.1 times its original value. For data augmentation, we incorporate random horizontal flips.

**Architecture details.** We use RGB images with dimensions of  $H \times W$ , which are  $1226 \times 370$  for SemanticKITTI and  $1408 \times 376$  for SSCBench-KITTI360. For the dimensions of  $\mathcal{F}^{3D}$ , denoted as  $X \times Y \times Z$ , we use  $128 \times 128 \times 8$ , which are subsequently upsampled to the scene resolution of  $256 \times 256 \times 32$ . We employ the pre-trained MaskDINO [29] weights to extract image features and use MobileStereoNet [28] to estimate a depth map for voxel query proposal, following Symphonies [12]. Lastly, the lightweight 3D UNet is composed by removing some 3D convolution layers from the 3D UNet as described in MonoScene [7]. For the hyperparameters in the VPZoomer, the zoom-in level  $\alpha$  is set to 0.2. In the VPCA module, we set the bound  $\beta$  to 30 and use scale factor  $c \in \{1, 1.5, 2.0\}$  in order, along the resolution of  $\mathcal{F}_o^{2D} \in \{1/4, 1/8, 1/16\}$ .

TABLE I: **Quantitative results on SemanticKITTI [16] test set.** <sup>†</sup> denotes the results provided by [6]. <sup>\*</sup> represents the reproduced results in [10], [12]. The highest results among camera-based methods are denoted in **bold**, and the second-highest results are underlined. The precision of decimals varies depending on the test values provided.

Method	Modality	IoU		mIoU		Precision (%)																	
		road	sidewalk	parking	other-grnd.	building	car	truck	bicycle	motorcycle	other-veh.	vegetation	trunk	terrain	person	bicyclist	motorcyclist	fence	pole	traf.-sign			
SSCNet <sup>†</sup> [3]	LiDAR	49.98	16.14	51.15	30.76	27.12	6.44	34.53	24.26	1.18	0.54	0.78	4.34	35.25	18.17	29.01	0.25	0.25	0.03	19.87	13.10	6.73	
LMSNet [6]	LiDAR	56.72	17.62	64.80	34.68	29.02	4.62	38.08	30.89	1.47	0.00	0	0.81	41.31	19.89	32.05	0	0	0	21.32	15.01	0.84	
SSC-RS [32]	LiDAR	59.7	24.2	73.1	44.4	38.6	17.4	44.6	36.4	5.3	10.1	5.1	11.2	44.1	26.0	41.9	4.7	2.4	0.9	30.8	15.0	7.2	
MonoScene* [7]	Camera	34.16	11.08	54.70	27.10	24.80	5.70	14.40	18.80	3.30	0.50	0.70	4.40	14.90	2.40	19.50	1.00	1.40	0.40	11.10	3.30	2.10	
TPVFormer [10]	Camera	34.25	11.26	55.10	27.20	27.40	6.50	14.80	19.20	3.70	1.00	0.50	2.30	13.90	2.60	20.40	1.10	2.40	0.30	11.00	2.90	1.50	
VoxFormer [8]	Camera	42.95	12.20	53.90	25.30	21.10	5.60	19.80	20.80	3.50	1.00	0.70	3.70	22.40	7.50	21.30	1.40	2.60	0.20	11.10	5.10	4.90	
OccFormer [11]	Camera	34.53	12.32	55.90	30.30	31.50	6.50	15.70	21.60	1.20	1.50	1.70	3.20	16.80	3.90	21.30	2.20	1.10	0.20	11.90	3.80	3.70	
SurroundOcc [33]	Camera	34.72	11.86	56.90	28.30	30.20	6.80	15.20	20.60	1.40	1.60	1.20	4.40	14.90	3.40	19.30	1.40	2.00	0.10	11.30	3.90	2.40	
Symphonies [12]	Camera	42.19	15.04	58.40	29.30	26.90	11.70	24.70	23.60	3.20	3.60	2.60	5.60	24.20	10.00	23.10	3.20	1.90	2.00	16.10	7.70	8.00	
VPOCC (Ours)	Camera	<b>44.09</b>	<b>15.65</b>	<b>59.10</b>	<b>32.30</b>	<u>30.90</u>	<u>9.70</u>	<b>26.30</b>	<b>24.40</b>	<b>5.30</b>	<u>3.30</u>	<b>3.20</b>	<b>5.60</b>	<b>25.90</b>	<u>9.70</u>	<b>25.70</b>	<u>2.40</u>	<b>2.90</b>	0.30	<b>17.20</b>	<u>6.60</u>	<u>6.30</u>	

TABLE II: **Quantitative results on SSCBench-KITTI360 [17] test set.** We refer to the results in [17], [12]. The highest results among the camera-based method are indicated in **bold**, and the second-highest results are underlined.

Method	Modality	IoU		mIoU		Precision (%)																	
		car	bicycle	motorcycle	truck	other-veh.	person	road	parking	sidewalk	other-grnd.	building	fence	vegetation	terrain	pole	traf.-sign	other-struct.					
SSCNet [3]	LiDAR	53.58	16.95	31.95	0.00	0.17	10.29	0.00	0.07	65.70	17.33	41.24	3.22	44.41	6.77	43.72	28.87	0.78	0.75	8.69	0.67		
LMSNet [6]	LiDAR	47.35	13.65	20.91	0.00	0.00	0.26	0.58	0.00	62.95	13.51	33.51	0.20	43.67	0.33	40.01	26.80	0.00	0.00	3.63	0.00		
MonoScene [7]	Camera	37.87	12.31	19.34	0.43	0.58	8.02	2.03	0.86	48.35	11.38	28.13	3.32	32.89	3.53	26.15	16.75	6.92	5.67	4.20	3.09		
TPVFormer [10]	Camera	40.22	13.64	21.56	1.09	1.37	8.06	2.57	2.38	52.99	11.99	31.07	3.78	34.83	4.80	30.08	17.52	7.46	5.86	5.48	2.70		
VoxFormer [8]	Camera	38.76	11.91	17.84	1.16	0.89	4.56	2.06	1.63	47.01	9.67	27.21	2.89	31.18	4.97	28.99	14.69	6.51	6.92	3.79	2.43		
OccFormer [11]	Camera	40.27	13.81	22.58	0.66	0.26	9.89	3.82	2.77	54.30	13.44	31.53	3.55	36.42	4.80	31.00	19.51	7.77	8.51	6.95	4.60		
Symphonies [12]	Camera	<b>44.12</b>	<b>18.58</b>	<b>30.02</b>	<u>1.85</u>	<b>5.90</b>	<b>25.07</b>	<b>12.06</b>	<b>8.20</b>	<b>54.94</b>	<u>13.83</u>	<u>32.76</u>	<b>6.93</b>	<u>35.11</u>	<b>8.58</b>	<b>38.33</b>	11.52	<u>14.01</u>	<u>9.57</u>	<b>14.44</b>	<b>11.28</b>		
VPOCC (Ours)	Camera	<b>46.69</b>	<b>19.54</b>	<u>28.44</u>	<b>3.92</b>	<b>6.68</b>	<u>19.15</u>	<u>9.94</u>	<u>6.21</u>	<b>59.82</b>	<b>16.62</b>	<b>37.94</b>	<u>5.23</u>	<b>42.04</b>	<u>8.31</u>	<u>37.51</u>	<b>21.69</b>	<b>15.03</b>	<b>17.45</b>	<u>9.52</u>	<u>6.29</u>		

TABLE III: **Quantitative results on SemanticKITTI [16] validation set.** <sup>\*</sup> represents the reproduced results in [10], [12]. The highest results are indicated **bold**, and the second-highest results are underlined.

Method	Modality	IoU		mIoU		Precision (%)																	
		road	sidewalk	parking	other-grnd.	building	car	truck	bicycle	motorcycle	other-veh.	vegetation	trunk	terrain	person	bicyclist	motorcyclist	fence	pole	traf.-sign			
MonoScene* [7]	Camera	36.86	11.08	56.52	26.72	14.27	0.46	14.09	23.26	6.98	0.61	0.45	1.48	17.89	2.81	29.64	1.86	1.20	0.00	5.84	4.14	2.25	
TPVFormer [10]	Camera	35.61	11.36	56.50	25.87	<b>20.60</b>	<u>0.85</u>	13.88	23.81	8.08	0.36	0.05	4.35	16.92	2.26	30.38	0.51	0.89	0.00	5.94	3.14	1.52	
VoxFormer [8]	Camera	44.02	12.35	54.76	26.35	15.50	0.70	17.65	25.79	5.63	0.59	0.51	3.77	24.39	5.08	29.96	1.78	<b>3.32</b>	0.00	7.64	7.11	4.18	
OccFormer [11]	Camera	36.50	13.46	<b>58.85</b>	26.88	<u>19.61</u>	0.31	14.40	25.09	<b>25.53</b>	0.81	1.19	8.52	19.63	3.93	<u>32.62</u>	2.78	<u>2.82</u>	0.00	5.61	4.26	2.86	
Symphonies [12]	Camera	41.92	14.89	56.37	27.58	15.28	<b>0.95</b>	<u>21.64</u>	28.68	20.44	<u>2.54</u>	<u>2.82</u>	<b>13.89</b>	<u>25.72</u>	<b>6.60</b>	30.87	<u>3.52</u>	2.24	0.00	<u>8.40</u>	<b>9.57</b>	<b>5.76</b>	
VPOCC (Ours)	Camera	<b>44.53</b>	<b>15.59</b>	<u>58.46</u>	<b>28.61</b>	17.91	0.36	<b>24.88</b>	<u>30.42</u>	18.51	<u>2.82</u>	<u>3.88</u>	<u>13.85</u>	<u>27.14</u>	<u>6.36</u>	<u>33.98</u>	<u>3.70</u>	2.36	<u>0.23</u>	<u>9.19</u>	<u>8.55</u>	<u>4.98</u>	

## B. Performance comparison

**Quantitative results.** As shown in Tabs. I, II, and III, we compare existing monocular 3D semantic occupancy prediction methods across different datasets: SemanticKITTI [16] and SSCBench-KITTI360 [17]. We outperform the previous best-performing models by showing performance improvements in both IoU (+1.14) and mIoU (+0.61) on SemanticKITTI test set, in IoU (+2.61) and mIoU(+0.70) on SemanticKITTI validation set, and in IoU (+2.57) and mIoU (+0.96) on SSCBench-KITTI360 test set. Unlike existing methods (*i.e.*, VoxFormer [8] and Symphonies [12]) that excel in only one metric, our approach surpasses previous methods in both the IoU and the mIoU

metrics on all datasets by creating a balanced feature volume over the scene using VP.

**Qualitative results.** In Fig. 5, we provide a qualitative comparison result for the SemanticKITTI validation set. Compared to VoxFormer and Symphonies, our VPOCC demonstrates sharp and distinguishable voxel shape in both near and far areas by addressing the information imbalance problem caused by the camera perspective geometry. For example, each boxed area shows that our approach enables the precise and sharp prediction of car shapes along the road by utilizing VP. Especially in the first column image, it is noticeable that only VPOCC constructs the tree and empty space in the distant areas.

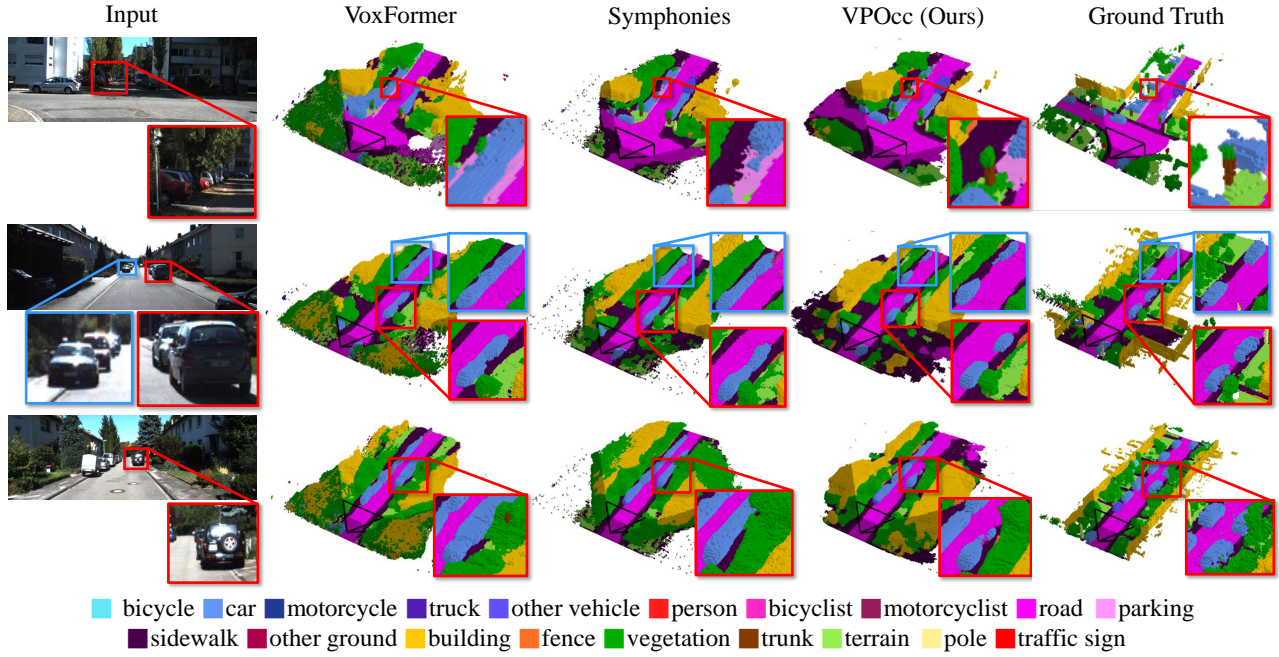


Fig. 5: **Qualitative results on SemanticKITTI validation set.** Our VPOcc shows better performance in the distant areas. We enlarge the boxed areas representing distant areas in the images.

TABLE IV: **Ablation and empirical studies of our proposed framework, VPOcc.**

(a) **Ablation study for the proposed framework.**

Method	VPZoomer	VPCA	BFVF	IoU	mIoU	Params (M)
Baseline				44.16	14.65	120.14
(1)	✓			44.14	14.49	120.14
(2)	✓	✓		43.78	14.89	120.34
(3)	✓		✓	<b>44.63</b>	<u>15.30</u>	125.22
VPOcc (Ours)	✓	✓	✓	44.53	<b>15.59</b>	125.21

(b) **Depth-wise performance evaluation**

Range	0m – 17m		17m – 34m		34m – 51.2m	
	IoU	mIoU	IoU	mIoU	IoU	mIoU
MonoScene [7]	39.05	12.49	38.52	12.22	31.83	8.57
TPVFormer [10]	37.89	12.94	37.24	11.67	30.72	8.46
VoxFormer [8]	<b>48.60</b>	12.95	46.83	13.85	35.85	9.54
OccFormer [11]	38.66	15.38	38.51	13.85	31.24	10.69
Symphonies [12]	39.71	<u>16.28</u>	<u>47.19</u>	<u>16.36</u>	38.04	<u>11.19</u>
VPOcc (Ours)	45.07	<b>17.02</b>	<b>48.89</b>	<b>17.04</b>	<b>39.03</b>	<b>11.83</b>

(c) **Empirical study for fusion strategy.**

Fusion	Sum	1×1 Conv	Gated [35]	BFVF(Ours)
IoU	43.78	<b>44.60</b>	44.48	<u>44.53</u>
mIoU	14.89	14.65	<u>15.34</u>	<b>15.59</b>

### C. Ablation studies

We conduct ablation studies on SemanticKITTI [16] validation set to validate our method.

**Architecture composition.** In this part, we validate the effectiveness of each sub-module: VPZoomer, VPCA, and BFVF modules. Tab. IV shows that each sub-component of

our framework contributes to the performance improvements in occupancy prediction and semantic segmentation. Compared to the baseline which is composed of the encoder, deformable cross-attention, and lightweight 3D UNet, we observe that adding VPZoomer leads to slight performance degradation in both IoU and mIoU. Because introducing VPZoomer also needs an effective fusion module for  $\mathcal{F}_o^{3D}$  and  $\mathcal{F}_z^{3D}$ , without the module, a naïve fusion (*i.e.*, summation) results in poor performance (*i.e.*, (1) vs. (3)). Besides, by resolving the problem at the aggregation level (2), we can observe the performance improvement in mIoU (+0.40). Lastly, when we effectively fuse two feature volumes that handle the perspective geometry effect in input and aggregation levels, we can get performance improvement in mIoU (+0.29). On the other hand, the modest disparity in the number of parameters between the baseline and VPOcc underscores the effectiveness of our modules.

**Depth-wise performance evaluation.** To validate the effectiveness of our framework for each depth range, we conduct the performance evaluation by partitioning the scene into thirds. As shown in Tab. IV-(b), we can observe the performance improvements not only in far areas but also in near areas, especially in terms of mIoU. Addressing the information imbalance issue could result in performance improvements across all distance ranges. Specifically, the limited receptive field of the encoder causes difficulty in aggregating the object-aware features from large and small object shapes (*i.e.*, near and far objects). However, thanks to our VPZoomer and VPCA modules that ensure the balanced information over the depth and geometry-considered aggregation, our method shows overall improvement for all depth ranges in IoU and mIoU. Note

that the second-best performance (*i.e.*, VoxFormer) explicitly uses an occupancy map as an input, leading to higher results of IoU in the  $0m - 17m$  range.

**Feature volume fusion.** To investigate effective voxel feature fusion design, we evaluate various strategies: naïve summation (*i.e.*, Sum), feature concatenation with  $1 \times 1$  convolution (*i.e.*,  $1 \times 1$  Conv), adaptive gated feature fusion (*i.e.*, Gated [35]), and our BFVF module. Tab. IV-(c) shows naïve summation is ineffective. Per-pixel fusion via  $1 \times 1$  Conv improves IoU (+0.82) but decreases mIoU by (-0.24) due to missing spatial fusion. The Gated module, using local attention, increases mIoU by (+0.69) but cannot handle the different spatial properties of  $\mathcal{F}_o^{3D}$  and  $\mathcal{F}_z^{3D}$ . Finally, the anisotropic convolution [31] in our BFVF module adaptively aggregates spatial information, achieving the highest performance mIoU metrics (+0.25).

## V. CONCLUSION

In this work, we propose VPOCC, a camera-based 3D semantic occupancy prediction framework utilizing VP to address the camera perspective geometry. Using VPZoomer, we can obtain balanced information for the entire scene by utilizing zoom-in images. Through VPCA, image features that are more suitable for 3D are aggregated by considering camera perspective projection. Finally, BFVF effectively fuses and refines the 3D feature volumes obtained from the original and zoom-in images. With the incorporation of these modules, VPOCC shows enhanced performance by handling information imbalance from camera perspective projection.

**Limitation.** As a limitation, the performance of VPOCC depends on VP accuracy. To address this, we test with a naïve VP estimation algorithm (details in the supplementary video) and find a performance drop, but still reasonable performance despite the decreased VP accuracy. Future work will aim to make the model more robust to VP variations.

## REFERENCES

- [1] L. Wang, H. Ye, Q. Wang, Y. Gao, C. Xu, and F. Gao, “Learning-based 3d occupancy prediction for autonomous navigation in occluded environments,” in *IROS*, 2021.
- [2] J. Crespo, J. C. Castillo, O. M. Mozos, and R. Barber, “Semantic information for robot navigation: A survey,” *Applied Sciences*, vol. 10, no. 2, p. 497, 2020.
- [3] S. Song, F. Yu, A. Zeng, A. X. Chang, M. Savva, and T. Funkhouser, “Semantic scene completion from a single depth image,” in *CVPR*, 2017.
- [4] D. Zou, P. Tan, and W. Yu, “Collaborative visual slam for multiple agents: A brief survey,” *Virtual Reality & Intelligent Hardware*, vol. 1, no. 5, pp. 461–482, 2019.
- [5] X. Yan, J. Gao, J. Li, R. Zhang, Z. Li, R. Huang, and S. Cui, “Sparse single sweep lidar point cloud segmentation via learning contextual shape priors from scene completion,” in *AAAI*, 2021.
- [6] L. Roldao, R. de Charette, and A. Verroust-Blondet, “Lmscnet: Lightweight multiscale 3d semantic completion,” in *2020 International Conference on 3D Vision (3DV)*, 2020.
- [7] A.-Q. Cao and R. de Charette, “Monoscene: Monocular 3d semantic scene completion,” in *CVPR*, 2022.
- [8] Y. Li, Z. Yu, C. Choy, C. Xiao, J. M. Alvarez, S. Fidler, C. Feng, and A. Anandkumar, “Voxformer: Sparse voxel transformer for camera-based 3d semantic scene completion,” in *CVPR*, 2023.
- [9] J. Yao, C. Li, K. Sun, Y. Cai, H. Li, W. Ouyang, and H. Li, “Ndcs-scene: Boost monocular 3d semantic scene completion in normalized device coordinates space,” in *ICCV*, 2023.
- [10] Y. Huang, W. Zheng, Y. Zhang, J. Zhou, and J. Lu, “Tri-perspective view for vision-based 3d semantic occupancy prediction,” in *CVPR*, 2023.
- [11] Y. Zhang, Z. Zhu, and D. Du, “Occformer: Dual-path transformer for vision-based 3d semantic occupancy prediction,” *arXiv preprint arXiv:2304.05316*, 2023.
- [12] H. Jiang, T. Cheng, N. Gao, H. Zhang, T. Lin, W. Liu, and X. Wang, “Symphonize 3d semantic scene completion with contextual instance queries,” in *Proceedings of the IEEE/CVF Conference on Computer Vision and Pattern Recognition*, 2024, pp. 20258–20267.
- [13] R. Hartley and A. Zisserman, *Multiple view geometry in computer vision*. Cambridge university press, 2003.
- [14] J. Dai, H. Qi, Y. Xiong, Y. Li, G. Zhang, H. Hu, and Y. Wei, “Deformable convolutional networks,” in *ICCV*, 2017.
- [15] X. Zhu, W. Su, L. Lu, B. Li, X. Wang, and J. Dai, “Deformable detr: Deformable transformers for end-to-end object detection,” *arXiv preprint arXiv:2010.04159*, 2020.
- [16] J. Behley, M. Garbade, A. Milioto, J. Quenzel, S. Behnke, C. Stachniss, and J. Gall, “SemanticKITTI: A dataset for semantic scene understanding of lidar sequences,” in *ICCV*, 2019.
- [17] Y. Li, S. Li, X. Liu, M. Gong, K. Li, N. Chen, Z. Wang, Z. Li, T. Jiang, F. Yu, *et al.*, “Sscbench: A large-scale 3d semantic scene completion benchmark for autonomous driving,” *arXiv preprint arXiv:2306.09001*, 2023.
- [18] Y. Wang, W.-L. Chao, D. Garg, B. Hariharan, M. Campbell, and K. Q. Weinberger, “Pseudo-lidar from visual depth estimation: Bridging the gap in 3d object detection for autonomous driving,” in *CVPR*, 2019.
- [19] J. Jiao, Y. Wei, Z. Jie, H. Shi, R. W. Lau, and T. S. Huang, “Geometry-aware distillation for indoor semantic segmentation,” in *CVPR*, 2019.
- [20] X. Li, Z. Jie, W. Wang, C. Liu, J. Yang, X. Shen, Z. Lin, Q. Chen, S. Yan, and J. Feng, “Foveanet: Perspective-aware urban scene parsing,” in *ICCV*, 2017.
- [21] X. Chen, K. Kundu, Y. Zhu, A. G. Berneshawi, H. Ma, S. Fidler, and R. Urtasun, “3d object proposals for accurate object class detection,” *NeurIPS*, 2015.
- [22] J. Lee, G. Cho, J. Park, K. Kim, S. Lee, J.-H. Kim, S.-G. Jeong, and K. Joo, “SlaBins: Fisheye Depth Estimation using Slanted Bins on Road Environments,” in *ICCV*, 2023.
- [23] Y. Liu, P. Sun, N. Wergeles, and Y. Shang, “A survey and performance evaluation of deep learning methods for small object detection,” *Expert Systems with Applications*, vol. 172, p. 114602, 2021.
- [24] M. Kisantal, Z. Wojna, J. Murawski, J. Naruniec, and K. Cho, “Augmentation for small object detection,” *arXiv preprint arXiv:1902.07296*, 2019.
- [25] X. Zhang, Q. Chen, R. Ng, and V. Koltun, “Zoom to learn, learn to zoom,” in *CVPR*, 2019.
- [26] C. Thavamani, M. Li, N. Cebron, and D. Ramanan, “Fovea: Foveated image magnification for autonomous navigation,” in *ICCV*, 2021.
- [27] A. Ghosh, N. D. Reddy, C. Mertz, and S. G. Narasimhan, “Learned two-plane perspective prior based image resampling for efficient object detection,” in *CVPR*, 2023.
- [28] F. Shamsafar, S. Woerz, R. Rahim, and A. Zell, “Mobilestereonet: Towards lightweight deep networks for stereo matching,” 2022.
- [29] F. Li, H. Zhang, H. Xu, S. Liu, L. Zhang, L. M. Ni, and H.-Y. Shum, “Mask dino: Towards a unified transformer-based framework for object detection and segmentation,” in *CVPR*, 2023.
- [30] Y. Zhou, H. Qi, J. Huang, and Y. Ma, “Neurvps: Neural vanishing point scanning via conic convolution,” *Advances in Neural Information Processing Systems*, vol. 32, 2019.
- [31] J. Li, K. Han, P. Wang, Y. Liu, and X. Yuan, “Anisotropic convolutional networks for 3d semantic scene completion,” in *CVPR*, 2020.
- [32] J. Mei, Y. Yang, M. Wang, T. Huang, X. Yang, and Y. Liu, “Ssc-rs: Elevate lidar semantic scene completion with representation separation and bev fusion,” in *2023 IEEE/RSJ International Conference on Intelligent Robots and Systems (IROS)*. IEEE, 2023, pp. 1–8.
- [33] Y. Wei, L. Zhao, W. Zheng, Z. Zhu, J. Zhou, and J. Lu, “Surroundoc: Multi-camera 3d occupancy prediction for autonomous driving,” in *Proceedings of the IEEE/CVF International Conference on Computer Vision*, 2023, pp. 21729–21740.
- [34] I. Loshchilov and F. Hutter, “Decoupled weight decay regularization,” *arXiv preprint arXiv:1711.05101*, 2017.
- [35] J. H. Yoo, Y. Kim, J. Kim, and J. W. Choi, “3d-cvf: Generating joint camera and lidar features using cross-view spatial feature fusion for 3d object detection,” in *ECCV*, 2020.